



Behavior Score Prediction in Resting-State Functional MRI by Deep State Space Modeling

Javier Salazar Cavazos[✉], Graduate Student Member, IEEE
 Maximillian Egan, Krisanne Litinas, Benjamin Hampstead[✉], and Scott Peltier[✉]

Abstract— Early clinical assessment of Alzheimer’s disease relies on behavior scores that measure a subject’s language, memory, and cognitive skills. On the medical imaging side, functional magnetic resonance imaging has provided invaluable insights into the neural pathways underlying Alzheimer’s disease. While prior studies have used resting-state functional MRI by extracting functional connectivity matrices, these approaches neglect the temporal dynamics inherent in functional data. In this work, we present a deep state space modeling framework that directly leverages the blood-oxygenation-level-dependent time series to learn a sparse collection of brain regions to predict behavior scores. Our model extracts temporal features that encapsulate nuanced patterns of intrinsic brain activity, thereby enhancing predictive performance compared to traditional connectivity methods. We identify specific brain regions that are most predictive of cognitive impairment through experiments on data provided by the Michigan Alzheimer’s Disease Research Center, providing new insights into the neural substrates of early Alzheimer’s pathology. These findings have important implications for the possible development of risk monitoring and intervention strategies in Alzheimer’s disease.

Index Terms— Alzheimer’s disease, behavior score prediction, deep learning, Mamba, Montreal cognitive assessment, resting-state functional magnetic resonance imaging, state space models.

I. INTRODUCTION

A. Background

Functional magnetic resonance imaging (fMRI), that consists of a series of volumetric brain MRI samples, has been explored in various contexts for insights into brain function [1]. The signal acquired, that being blood-oxygen-level-dependent (BOLD) data, is used as a proxy for neural activity that impacts

Received X February 2026. This work was supported by U.S. National Institutes of Health (NIH) under Grant R21 AG082204, by the National Institute on Aging (NIA) via Michigan Alzheimer’s Disease Research Center (MADRC; P30 AG072931), and by the University of Michigan under the Rackham Merit Fellowship (RMF) award.

Javier Salazar Cavazos is with the Electrical and Computer Engineering (ECE) Department, University of Michigan, Ann Arbor, MI 48109 USA (e-mail: javiersc@umich.edu); Maximillian Egan, Krisanne Litinas, and Scott Peltier are with the Functional MRI Laboratory, Departments of Radiology and Biomedical Engineering (BME), University of Michigan, Ann Arbor, MI 48109 USA (e-mail: mkegan@umich.edu; klitinas@umich.edu; spelt@umich.edu); Benjamin Hampstead is with the Michigan Alzheimer Disease Research Center (MADRC) and Research Program on Cognition and Neuromodulation Based Interventions (RPCNBI), Departments of Psychiatry and Neurology, University of Michigan, Ann Arbor, MI 48109 USA (e-mail: bhampste@umich.edu).

hemodynamics at a voxel level. Resting-state fMRI (rs-fMRI) is a neuroimaging technique that measures spontaneous brain activity by detecting regional differences in cerebral blood flow while a person is not performing any explicit task under the scanner. It is important because it reveals patterns of functional connectivity between brain regions, providing insights into brain organization and various neurological or psychiatric conditions [2]. These patterns indicate correlated brain activations that can reflect physiological changes in the brain [3], [4]. Recent works have focused on identifying neurological diseases using machine learning models based on functional connectivity [5], [6], which is a technique that measures correlations of BOLD activity among brain regions. Further, various works have shown that the default mode network (DMN), a collection of brain regions active when a person is not performing a specific task in rs-fMRI, consists of a baseline state that involves self-referential processing and internal directed cognition [7], [8]. In this work, we explore whether the default mode network plays a significant role in cognitive impairment through behavior score prediction.

Alzheimer’s disease (AD) is a progressive neurodegenerative disease that often leads to dementia that is characterized by loss of cognitive and memory function. Healthy patients are known as cognitively normal (CN) and clinicians have classified Alzheimer’s disease into three distinct stages: the preclinical stage, an intermediate phase known as mild cognitive impairment (MCI), and, in the later stages, dementia of the Alzheimer’s type (DAT) [9]. Preclinical AD affects the brain years before any diagnosis is made and so there is a need to study brain changes in the early stages to aid detection and treatment methods. Unfortunately, there are often confounders or mixed pathologies, e.g., depression or Parkinson’s disease [10], that complicate the diagnosis process. This places high importance for adaptable biomarkers that can differentiate overlapping pathologies such as fMRI, positron emission tomography (PET), and others. The first and most viable diagnostic marker, meaning cheapest and easiest to implement, is one that does not require any imaging such as a written cognitive exam that tests for things such as memory, language, and general cognition. The primary cognitive measure, also called a behavior score, analyzed in this work is the Montreal Cognitive Assessment (MoCA) that is designed for screening MCI subjects that has been shown superior to other exams such as the Mini-Mental State Examination (MMSE) [11]. The MoCA exam includes tasks on several areas like short-term

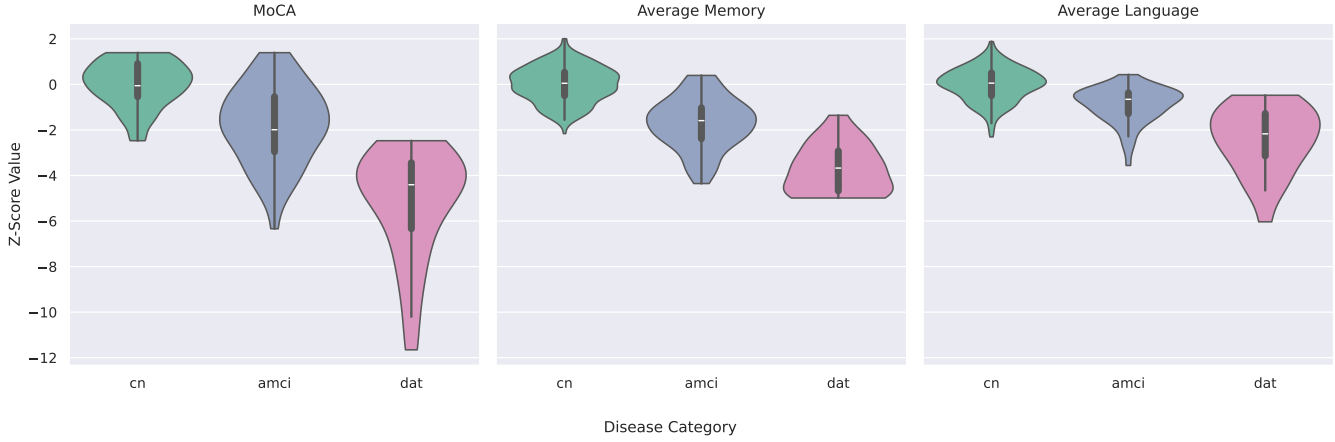


Fig. 1: Violin plots illustrating the distribution of behavioral scores in z-score space across different disease categories.

memory recall, delayed recall, visual spatial, executive function, sustained attention, language, and time/place orientation. MoCA can discriminate between MCI and CN subjects with an area under the curve (AUC) of 0.86 indicating the practicality of this metric for early diagnosis [11]. Additionally, in this work we also compute average memory and language metrics for the prediction task. Incorporating these average subcategories with the MoCA metric provides finer detailed information on subject cognitive performance.

B. Related Works

The intersection between behavior score prediction and imaging modalities is not entirely unprecedented. For example, the brain-behavior relationship has been studied in PET imaging using standardized uptake value ratio (SUVR) features [12]. More closely to this work, the association with MoCA and depression subjects has been studied in a rs-fMRI context [13] by using the functional connectivity predictive modeling (CPM) method [14]. In terms of behavior score prediction and AD subjects, Ref. [15] predicts the ADAS-Cog [16] metric using CPM on subjects spanning the AD spectrum. Further, Ref. [17, Chapter 2] does something similar with functional connectivity data using the CPM method in a cohort of purely MCI subjects. The Pearson correlation coefficient (R) for MoCA prediction is 0.07 in Ref. [17, Chapter 2] and 0.15 in Ref. [13] indicating a fairly weak correlation for MoCA prediction in rs-fMRI. It is worth noting that this is not a completely fair comparison since these works use different rs-fMRI datasets and methodologies. However, these works only consider functional connectivity data which collapses the time dimension and instead only looks at brain region interactions. To the best of the authors' knowledge, there are no works that tackle behavior score prediction on the BOLD timeseries data itself which may provide richer context to finding more optimal predictions. Furthermore, these works do not investigate cognitive subcategories such as memory and language in this prediction problem, only broad metrics such as MoCA.

Category	Total Subjects	Race (W/B/A)	Sex (M/F)	Average MoCA
CN	203	169/31/3	132/71	27.1
aMCI	53	44/8/1	16/37	23.5
DAT	25	24/0/1	12/13	16.3

TABLE I: Distribution of subjects in the MADRC dataset, stratified by disease category.

C. Contributions & Motivation

In recent brain stimulation research, Ref. [18] utilized high-definition transcranial direct current stimulation (HD-tDCS) to target exclusively the left ventrolateral prefrontal cortex in individuals with mild cognitive impairment (MCI). This intervention was administered in a double-blind protocol alongside either mnemonic strategy training or autobiographical recall control conditions over the course of five consecutive daily sessions. The findings demonstrate pronounced neurophysiological effects during associative memory encoding in the experimental group relative to controls. These results underscore the significance of delineating specific brain regions implicated in cognitive impairment, informing the potential for HD-tDCS applications in AD that extend beyond single-region stimulation paradigms.

In this work, we systematically contrast the rs-fMRI modality for behavior score prediction in subjects spanning the AD spectrum for MoCA and subcategory metrics. This is done by exploring both functional connectivity and multivariate timeseries methods for this task, developing a data-driven deep learning method based on state space models that outperforms the other approaches, and drawing biological insights related to the brain-behavior relationship.

II. DATA ACQUISITION & PROCESSING

A. Dataset

The Michigan Alzheimer's Disease Research Center (MADRC), in collaboration with University of Michigan, has collected functional and structural 3T MRI single session scans along with behavior score metrics for use in this project as part of the National Institute on Aging (NIA) grant P30 AG072931. All participants provided written informed consent and study activities were approved by respective parties. Resting-state

fMRI scans were completed eyes open with a fixation cross. The 3T rs-fMRI data is acquired with a multi-band (MB) echo-planar imaging (MB-EPI) pulse sequence with MB factor of 6 leading to a 30ms echo time (TE), 0.8s repetition time (TR), a flip angle of 52°, a 2.4mm spatial resolution, 60 total slices, and 570 total time samples.

The MADRC subject population consists of a total of 281 subjects across all disease category labels. For additional details, see Table I for demographic characteristics. Table acronyms are listed as follows: CN = cognitively normal, aMCI = amnestic mild cognitive impairment, DAT = Dementia of the Alzheimer's Type, W = White/Caucasian, B = Black/African American, A = Asian, M = Male, and F = Female. The behavior score distribution among subjects is illustrated in Fig. 1 by disease category and behavior score subcategories.

B. Behavior Score Metrics

As stated earlier, the MoCA score is the main cognitive metric used in this work. Additionally, memory and language submetrics are computed to provide a deeper understanding of cognitive impairment. In greater detail, a composite memory metric was calculated, averaging the z-scores of the UDS Benson complex figure recall [19], CRAFT story delayed recall [20], and CRAFT delayed verbal [20] behavioral tasks. A composite language metric was calculated, averaging the z-scores of total numbers of named animals [19], total number of named vegetables [19], and the Multilingual Naming Test (MINT) exam [21]. All metrics are z-score normalized based on the healthy population data.

C. Preprocessing

First, the raw data is processed by converting it to the standard BIDS format [22] to be used in downstream software packages. Secondly, the application fmriprep [23] handles most standard tasks such as N4 bias field correction, skull stripping, normalization to the MNI152 linear space provided by the TemplateFlow archive [24], head-motion estimation, susceptibility distortion correction using fieldmaps, and z-score normalization of each voxel's timeseries data.

Secondly, the CONN toolbox [25] then applies a 6mm FWHM Gaussian smoothing kernel, detrending (quadratic), despiking (loess regression smoothing, piecewise cubic interpolation), nuisance regression (motion parameters by first derivative and quadratic modeling, cerebral spinal fluid and white components identified by PCA in masks), outlier scan removal, and bandpass filtering between 0.008-0.09Hz.

Lastly, the BOLD data is parcellated into 264 regions of interest (ROIs) using the Power atlas [26], with 8 additional ROIs we manually included ourselves to augment the atlas since some areas of the amygdala and hippocampus may not be sufficiently covered; giving a total of 272 ROIs used in this project. The MNI coordinates and labels for these additional ROIs are included in Table II. Please see github.com/javiersci/NeuroMamba for additional information regarding our specific fmriprep and CONN toolbox preprocessing pipeline.

ROI	MNI (x, y, z)	Label
265	(-24, -4, -20)	Left Amygdala
266	(24, -2, -20)	Right Amygdala
267	(28, -12, -20)	Right Hippocampus
268	(30, -24, -12)	Right Hippocampus
269	(30, -39, -3)	Right Hippocampus
270	(-29, -12, -22)	Left Hippocampus
271	(-30, -24, -12)	Left Hippocampus
272	(-29, -38, -4)	Left Hippocampus

TABLE II: MNI coordinates and anatomical labels for additional regions of interest (ROIs) incorporated alongside the 264 ROIs defined in the Power atlas.

III. FORMULATION & RELATED METHODS

A. Problem Formulation

For each subject i , a 3D volume is acquired over time to get BOLD data $V^i \in \mathbb{R}^{T \times S_X \times S_Y \times S_Z}$ where T represents time and (S_X, S_Y, S_Z) are spatial dimensions. After the preprocessing outlined in Sec. II, the timeseries data becomes $X^i \in \mathbb{R}^{T \times B}$ where $B = 272$ refers to the brain region ROIs and $T = 570$ represents time samples. This timeseries data X^i will be the main focus of this work.

The goal then is to find some function $g(\cdot)$ that maps the given input, either X^i or some derivative of it, to the output $s^i \in \mathbb{R}^3$ where s^i represents the MoCA, memory, and language metrics for the i th subject. In this section, different methods are introduced that extract features from X^i to be used in a regression model setting. We start with discussion on functional connectivity in Sec. III-B.

B. Functional Connectivity

1) **Functional Connectivity Matrix (FCM):** One can generate functional connectivity data by forming the Pearson product-moment correlation coefficient matrix using X^i . Let $C^i \in \mathbb{R}^{B \times B}$ represent the functional connectivity matrix. Mathematically, this is computed by

Functional Connectivity Matrix (FCM)

$$\forall j, k \in \mathcal{B}, \quad C_{j,k}^i = \frac{\text{cov}(X_{:,j}^i, X_{:,k}^i)}{\sigma(X_{:,j}^i) \sigma(X_{:,k}^i)} \quad (1)$$

where \mathcal{B} is the set of brain regions, $\text{cov}(\cdot)$ is covariance, and $\sigma(\cdot)$ is standard deviation. These connectivity values, C^i , are used as features in a kernel ridge regression setup as further discussed in Sec. III-B.2.

2) **Kernel Ridge Regression (KRR):** Since the functional connectivity matrix is symmetric, the upper half is extracted by the linear operator \mathcal{A} such that $\mathcal{A}(C_i) \in \mathbb{R}^{\tilde{B}}$ is a vector whose elements are the brain region correlations and where $\tilde{B} = B(B - 1)/2$. Let $R \in \mathbb{R}^{N \times \tilde{B}}$ such that the rows of R represent different subjects, i.e., $R = [\mathcal{A}(C_1), \dots, \mathcal{A}(C_N)]'$. Given this matrix R , the goal is to find a mapping $g : g(R) \rightarrow S \in \mathbb{R}^{N \times 3}$ where S contains all behavior score metrics across subjects.

In standard ridge regression [27], the objective is to minimize the loss function with a regularization term to prevent

overfitting by minimizing

$$\min_{W,B} \underbrace{\frac{1}{2} \|S - RW - B\|_F^2}_{\text{data fidelity}} + \lambda \underbrace{\|W\|_F^2}_{\text{prevent large values}} \quad (2)$$

where $\|\cdot\|_F$ is the Frobenius norm, W are the regression weights, B is the bias term, and $\lambda > 0$ is the regularization parameter. In (2), $g(R) = RW + B$ is the model assumption for R . To extend this approach, kernel ridge regression (KRR) [28] replaces the inner product of feature vectors with a kernel function $k(\cdot, \cdot)$, implicitly mapping inputs into a higher dimensional space defined by the kernel. The kernel matrix $K \in \mathbb{R}^{N \times N}$ is computed such that $K_{i,j} = k(R_{i,:}, R_{j,:})$. The KRR model optimizes the following objective

Kernel Ridge Regression (KRR)

$$\min_{W,B} \underbrace{\frac{1}{2} \|S - KW - B\|_F^2}_{\text{data fidelity}} + \lambda \|KW\|_F^2. \quad (3)$$

In our experiments, we use the radial basis function (RBF) kernel, also called the Gaussian kernel, defined as

$$k(R_{i,:}, R_{j,:}) = \exp(-\gamma \|R_{i,:} - R_{j,:}\|_2^2) \quad (4)$$

where $\gamma > 0$ is the kernel hyperparameter that controls the width or spread of the kernel. A larger γ means the kernel declines rapidly with distance focusing more on close neighbors while a smaller γ makes the kernel smoother and more global. The RBF kernel is the most widely used kernel function in machine learning because of its versatility and strong performance on a wide variety of tasks [29]. By using it, the model can capture nonlinear relationships between functional connectivity and score metrics, thereby improving predictive accuracy. From (3), it should be clear that different weights and bias terms are computed for each behavior score metric given the same functional connectivity data. In Sec. III-C, multivariate timeseries modeling methods are discussed as an alternative to functional connectivity.

C. Model-Based Timeseries

1) *Individual Independent Component Analysis (I-ICA)*: Independent component analysis (ICA) [30] has become a fundamental tool in fMRI research for decomposing BOLD timeseries data into spatially independent components representing distinct functional networks [31]. ICA enables the identification of both task-based and resting-state networks without prior knowledge of temporal profiles, making it particularly valuable for exploratory analyses. To give a few examples, some common applications are the isolation of resting-state networks such as the default mode network [31], characterization of brain connectivity changes in neurological and psychiatric conditions [32], and the separation of physiological noise or motion artifacts from true neural signals [33]. In our experiments, we use ICA to extract features from the multivariate timeseries data X^i .

ICA, similar to principal component analysis (PCA), is a method where one finds a low-dimensional feature space

that consists of independent sources/components and mixing coefficients that maximizes the mutual information between the feature space and ambient space. The model assumes that $X = ME$ where M are the mixing coefficients and E are the independent sources/components. The goal is to find the inverse mapping $W = M^{-1}$ so given the original data X , one finds the components by unmixing, i.e., $E = WX$. Mathematically, given timeseries data $\tilde{X} \in \mathbb{R}^{T \times B}$ that has zero mean and unit covariance, ICA is associated with the following objective

Independent Component Analysis (ICA)

$$\min_{W} \underbrace{\frac{1}{2} \|a(W\tilde{X})\|_F^2}_{\text{sparsity regularizer}} \quad \text{s.t.} \quad \underbrace{WW'}_{\text{orthonormal sources}} = I \quad (5)$$

where W contains the inverse mixing coefficients, $W\tilde{X}$ are the components, a is a nonlinear convex function such as $\log(\cosh(\cdot))$, and $WW' = I$ is the independent constraint. This is done for each subject independently to extract the components, and we denote this version as individual ICA (I-ICA). In this work, the components are features used in conjunction with KRR as the regression model by solving (3) on the input $\hat{W}\tilde{X}$ where \hat{W} is the solution to solving (5) and \tilde{X} is whitened version of X .

2) *Group Independent Component Analysis (G-ICA)*: In classical ICA for fMRI, labeled here as I-ICA, each subject has components extracted independently from each other which can result in inconsistencies among multiple subjects. The classical ICA method does not generalize to draw inferences about groups of subjects since different subjects will have different time courses so it is not immediately clear how to extend the method for group data [34]. Thus, modifications are required to make the method more meaningful in a group context; many approaches have been developed for this in the fMRI context [34]. The most widely used group ICA method is a temporal concatenation approach known as GIFT/MELODIC [35] where a matrix $G \in \mathbb{R}^{TN \times B}$ is formed that consists of temporally stacked data for all subjects. This ensures common sources are found across the population. Let \mathcal{T}_i represent the set of all time samples associated with subject i and W_G is the result of solving (5) on \tilde{G} , a whitened version of G . Each subject contains a submatrix $W_{G_i} = W_G[\mathcal{T}_i, :]$ in W_G that contains the unmixing coefficients. Similarly as before, the components $\hat{W}_{G_i}\tilde{X}^i$ are extracted from W_G for all subjects and used in KRR as the regression model by solving (3).

3) *Amplitude of Low Frequency Fluctuations (ALFF)*: The amplitude of low frequency fluctuations (ALFF) is a metric derived from BOLD timeseries data that extracts Fourier coefficients. ALFF quantifies the intensity of activity by measuring the power spectral density of low frequency fluctuations for each brain region timeseries signal. Higher ALFF values indicate greater regional neural activity, providing insights into baseline brain function and potential alterations associated with neuropsychiatric conditions. To give a few examples, this method was used to predict mini mental state exam (MMSE) scores for subjects in the AD spectrum ($R = 0.21$) [36],

predict frequency of migraines in individuals ($R = 0.35$) [37], and identify brain regions relevant in schizophrenia subjects [38]. Mathematically, for each subject i , this method computes

Amplitude of Low Frequency Fluctuations (ALFF)

$$a^i = \left[\mathcal{M}(|\mathcal{Z}(\mathcal{F}(X_{b,:}^i))|^{1/2}) \text{ for } b \in \{1, \dots, B\} \right] \quad (6)$$

where $\mathcal{M}(\cdot)$ computes the mean, $\mathcal{Z}(\cdot)$ extracts the Fourier coefficients associated with frequencies 0.008-0.9Hz, $\mathcal{F}(\cdot)$ is the Fourier transform, and $|\cdot|$ computes the magnitude of the complex coefficients. The ALFF of all subjects is computed to form $A = [a_1, \dots, a_N]^T \in \mathbb{R}^{N \times B}$. This matrix of ALFF features, computed using (6), is given as input to KRR as the regression model by solving (3).

D. Data-Driven Timeseries

1) *Temporal Convolutional Network (TCN)*: Temporal Convolutional Networks (TCNs) [39] are deep models designed specifically for processing sequential data. They are based on convolutional neural networks (CNNs), which are well-known for their efficiency in processing visual data such as images. In TCNs, the convolutional layers are applied along the time dimension of the sequential data. This model is adapted for regression by changing the head to instead perform global average pooling along the time dimension and adding a linear layer to predict behavior scores from the number of channels or variates in this instance.

2) *Long Short-Term Memory (LSTM)*: Long short-term memory networks (LSTMs) [40] are a specialized type of a recurrent neural network (RNN) designed to address the vanishing and exploding gradient problems commonly encountered in standard RNNs. By incorporating gated memory cells, LSTMs are able to effectively capture and utilize long-range dependencies in sequential data, making them highly successful for a variety of tasks. This is due to their use of input, output, and forget gates, which allow the model to selectively retain relevant information over extended sequences. Since their introduction, LSTMs have served as a foundational building block for many advances in sequence modeling and have inspired a range of related architectures. In our experiments, a bidirectional variant [41] of the LSTM model is used and denoted as “BiLSTM”. This architecture is adapted for regression similar to the TCN model.

3) *Patch Time Series Transformer (PatchTST)*: The Patch Time Series Transformer (PatchTST) [42] adapts the Transformer architecture [43] for time series tasks by introducing a patch-based input representation. Unlike traditional approaches that operate on individual time steps, PatchTST partitions the input sequence into a set of overlapping patches, enabling the model to capture both local and global patterns efficiently. This design leverages self-attention mechanisms to model complex temporal dependencies across multiple variables. PatchTST has achieved excellent performance on multivariate time series forecasting tasks [42], demonstrating improved performance over classical Transformer models.

This architecture is adapted for regression similar to the TCN model.

IV. PROPOSED METHOD

A. Deep State Space Models (SSMs)

State space models (SSMs) model physical systems through state variables that track how inputs change system behavior over time and can be written in matrix form for linear and time-invariant (LTI) systems [44]. Given an input signal $x(t) \in \mathbb{R}$, the SSM will generate an output sequence $y(t) \in \mathbb{R}$ using the state $h(t) \in \mathbb{R}^L$ by equations

$$\begin{aligned} h'(t) &= Ah(t) + Bx(t) \\ y(t) &= Ch(t) + Dx(t) \end{aligned} \quad (7)$$

where A is the state matrix, B is the input matrix, C is the output matrix, D is the feedthrough matrix, and L is the state size. In well-known physical problems, the $\{A, B, C, D\}$ matrices are known through differential equations or physics modeling that describe the system. In contrast, for complex systems, the dynamics are either unknown or difficult to model, so the $\{A, B, C, D\}$ matrices are learned in a data-driven way in the deep SSM context. The first popular work that studies this deep SSM idea and addresses some important challenges such as matrix initialization and fast parallelized computation is the structured SSM (S4) model [45]. Since acquired data is discrete with some time step Δ , the recurrence equation in (7) is rewritten using zero-order hold discretization [46] by

S6 Block

$$\begin{aligned} \bar{A} &= \exp(\Delta A), \quad \bar{B} = (\Delta A)^{-1}(\exp(\Delta A) - I) \cdot \Delta B, \\ y_k &= Ch_t, \quad h_t = \bar{A}h_{t-1} + \bar{B}x_t. \end{aligned} \quad (8)$$

Note that D is dropped since it can easily be implemented as a skip connection in a neural network context. Note that both (7) and (8) are for a single sequence, and so to process multiple variates, multiple independent SSM instances are used in practice.

However, since the SSM modeling in (7) and (8) is time-invariant, this poses challenges for certain tasks such as noun selection in language problems. Thus, the S6 layer, named after S4 combined with selective scanning, employs a selective mechanism, where $\{A, B, C\}$ are time-varying so the SSM is content-aware [46], [47]. However, since the system is no longer LTI, the update rules for $\{A, B, C\}$ can no longer be easily parallelized in FFT multiplication form. Instead, the recurrence equation is used but still efficiently parallelized by parallel scan methods also known as parallelized prefix sum algorithms [48]. Additionally, the S6 layer remains linear so in practice the layer is wrapped around a “Mamba block” formalized by

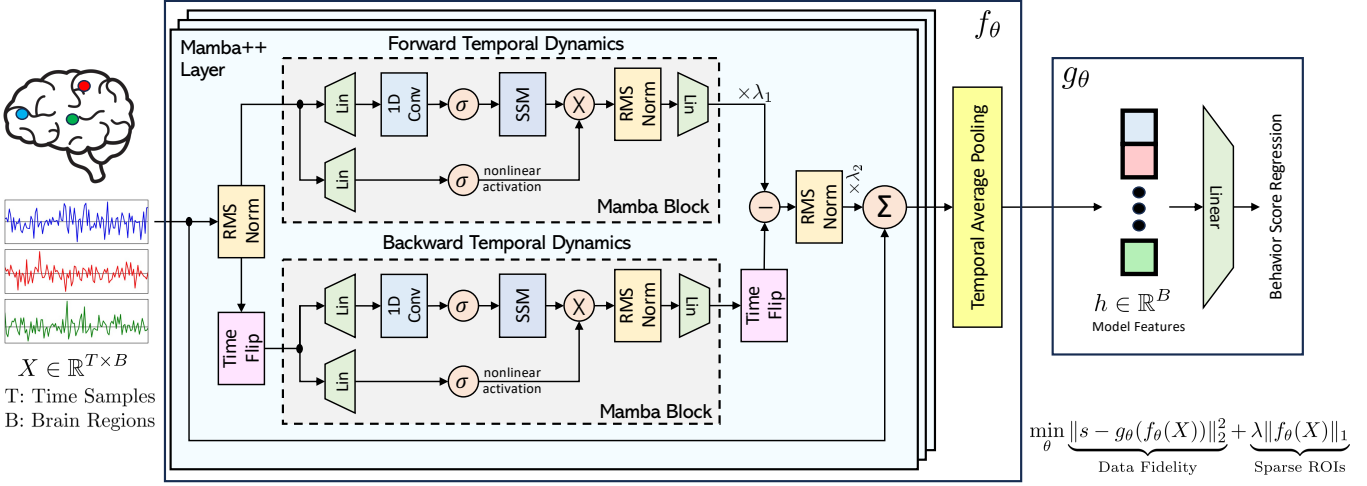


Fig. 2: Overview of the proposed NeuroMamba architecture for behavior score prediction using deep state space modeling. The Mamba++ layer extracts temporal features from each brain region relevant to prediction. Temporal averaging is subsequently applied to derive a single scalar summary statistic per region, which is then processed by a linear head.

Mamba Layer

$$\begin{aligned} H &= \sigma(\text{Conv1D}(\text{Affine}(X))), \quad Z = \sigma(\text{Affine}(X)), \\ Y &= \text{S6}(H), \quad \hat{Y} = \text{Affine}(Y \odot Z) \end{aligned} \quad (9)$$

where X is the input, \hat{Y} is the output, σ is SiLU activation, $\text{S6}(\cdot)$ is the operation in (8), and \odot is element-wise multiplication with the gating mechanism Z . This time-varying S6 layer, wrapped around nonlinear components, allows for a non-LTI SSM formulation that can better capture the nuances of complex systems that do not satisfy linearity nor time-invariance. However, this Mamba model was primarily designed for language tasks, and so does not take advantage of domain-specific knowledge such as multivariate timeseries data. In Sec. IV-B, modifications to the Mamba model are proposed such as bidirectionality and differential design to aid with modeling temporal dynamics in the timeseries data.

B. NeuroMamba

1) Bidirectionality: To enhance Mamba’s ability to preserve historical information in a longer range, we generalize by introducing two mamba blocks, one to capture forward temporal dynamics and another for backward temporal dynamics. This addresses the limitation of SSMs forgetting past information at longer lengths [49] by focusing both on recent and past information. We note that this kind of idea is not novel as similar ideas have already been proposed for long short-term memory networks (LSTMs) and others [41]. The Mamba model does not have this functionality because it was designed for language tasks where the goal is to auto-regressively predict the next token in a left-to-right fashion. However, in this fMRI application, one is more interested in learning from the temporal dynamics to predict behavior scores, and because this is not a model for real-time use, bidirectionality allows for a more predictive model in this offline context.

2) Differential design: Sequence models such as Transformers and RNNs tend to overallocate attention to irrelevant context, especially for multi-needle retrieval language tasks where the goal is to answers embedded in a pile of documents. Recent works focused on differential attention [50] to calculate the difference between two attention mechanisms, and this was found to cancel noisy intermediate representations similar to differential amplifiers in electrical engineering. This led to advantages in key information retrieval, hallucination mitigation, in-context learning, and reduction of activation outliers [50]. This idea has been recently extended to RNNs and SSMs [51]. We incorporate this idea because of similarities to our problem, e.g., finding a few variates embedded within the entire list that are most impactful for prediction similar to multi-needle retrieval. Because this differential design never performed worse than the baseline model [50], we integrate this idea with bidirectionality to instead calculate the learnable scaled difference as opposed to simply taking the addition of the two Mamba blocks.

3) Small Batch Regularization (SBR): Neural networks with strong performances are almost always overparameterized, hence why they are called “deep”. Despite explicit regularization to avoid overfitting, some studies have analyzed that the implicit regularization of small batch training tends to converge to minimas that have better generalization performance regardless if explicit regularization is used [52]–[54]. Specifically, under limited training samples the regularization effect remains strong [52] and training with multiple dataset passes, also called epochs, is theoretically optimal relative to single pass training [54]. We incorporate this small batch regularization (SBR) idea to train our model in order to achieve higher generalization performance and to prevent overfitting on our limited sample size dataset.

4) Model Overview: Putting everything together, the bidirectionality and differential design ideas are integrated to form an updated “Mamba++” layer utilized in the NeuroMamba model.

This layer is described by taking some input feature F from the last layer and performing the following

Mamba++ Layer

$$\begin{aligned}\tilde{F}_F &= \text{Mamba}(F), \quad \tilde{F}_B = \mathcal{T}(\text{Mamba}(\mathcal{T}(F))) \\ F_O &= \lambda_\theta^2 \odot \text{RMSNorm}(\lambda_\theta^1 \odot \tilde{F}_F - \tilde{F}_B) + F \quad (10)\end{aligned}$$

where $\lambda_\theta^1, \lambda_\theta^2 \in \mathbb{R}^B$ are learnable scaling parameters, $\text{RMSNorm}(\cdot)$ is root mean square normalization [55], and $\mathcal{T}(\cdot)$ is the linear operator for time flipping. Once the sequence has been processed by the Mamba++ layers, it is temporally averaged to summarize session statistics for every brain region. This forms a latent vector $h \in \mathbb{R}^B$ that is fed to an affine layer for score prediction. Let $f_\theta(\cdot)$ denote the NeuroMamba backbone that consists of a stack of Mamba++ layers combined with the temporal average pooling linear operator $\mathcal{P}(\cdot)$, $g_\theta(\cdot)$ denote the readout function that is simply an affine layer for linear regression, and θ correspond to the set of learnable parameters. Then, the NeuroMamba model is summarized by

NeuroMamba

$$f_\theta(\cdot) = \mathcal{P}([\text{Mamba}^{++}_\theta^{(l)}(\cdot) \text{ for } l = 1 \dots L]) \quad (11)$$

$$g_\theta(\cdot) = W_\theta f_\theta(\cdot) + b_\theta \quad (12)$$

$$\min_\theta \sum_{i=1}^N \underbrace{\frac{1}{2} \|s - g_\theta(f_\theta(X^i))\|_2^2}_{\text{data fidelity}} + \lambda \underbrace{\|f_\theta(X^i)\|_1}_{\text{sparse brain regions}} \quad (13)$$

where (13) is the cost function used to find optimal model parameters, s contains the behavior score metrics, and $\|\cdot\|_1$ is an L1 penalty term to promote a sparse number of brain regions that are relevant for prediction. See Fig. 2 for a pictorial representation of the NeuroMamba model. The code associated with all of these methods and experiments in this paper is published at github.com/javiersc1/NeuroMamba. In Sec. V, the experimental setup and results of these methods are discussed.

V. RESULTS & DISCUSSION

A. Setup

Due to the limited size of our dataset and the need to ensure generalization across the full distribution, we adopt a leave-one-out approach. Specifically, for each fold, the methods are trained on all data except one sample, which is held out for testing. This practice is commonly used in related fMRI prediction studies [13], [15], [17]. The $\{\text{FCM}, \text{I-ICA}, \text{G-ICA}, \text{ALFF}\}$ algorithms perform feature extraction by optimizing a convex cost function, and subsequently employ kernel ridge regression (KRR), which is also a convex optimization. Consequently, these methods are run until the optimization process converges. In contrast, the deep learning approaches $\{\text{TCN}, \text{BiLSTM}, \text{PatchTST}, \text{NeuroMamba}\}$ involve non-convex optimization and are therefore trained for a fixed number of 50 epochs, as further epochs yield minimal improvements in the cost function at this stage for all methods.

Method	MoCA	Memory	Language
FCM + KRR	0.07	0.08	0.10
I-ICA + KRR	0.14*	0.09	0.10*
G-ICA + KRR	0.18**	0.12*	0.16**
ALFF + KRR	0.20***	0.13*	0.18**
TCN	0.26***	0.16**	0.17**
BiLSTM	0.19***	0.19***	0.18**
PatchTST	0.28***	0.17**	0.19***
NeuroMamba	0.36***	0.24***	0.25***

TABLE III: Pearson correlation coefficients (R) and corresponding p-values (p) by score category for multiple methods applied to the MADRC rs-fMRI data. Asterisks denote statistical significance as follows: * = $p < 0.1$, ** = $p < 0.01$, *** = $p < 0.001$.

The Adam optimizer is used for training with momentum coefficients ($\beta_1 = 0, \beta_2 = 0.95$) meaning it behaves similar to RMSProp. Additionally, gradient clipping is used for the recurrent networks to prevent exploding gradients. All relevant hyperparameters for the various methods were determined via cross-validation using a randomly selected training/validation split of 50%/50%, ensuring that the chosen parameters are representative of the overall dataset. To promote fair assessment of model generalizability, these parameters remain fixed across all folds and are not re-optimized for each individual fold.

B. Experiments

1) *Predictive Accuracy:* In this experiment, the accuracy of different approaches are compared by analyzing the Pearson correlation coefficient (R) and associated p -values between the predicted and true behavior scores for each cognitive subcategory. In Table III, the R values are reported for MoCA, average memory, and average language for each method; for brevity, only the MoCA R values are discussed below. As demonstrated, the functional connectivity method (FCM) achieves $R = 0.07$ which closely aligns with published literature values of $R = 0.07$ [17] and $R = 0.15$ [13]. This is not a fair comparison given the different datasets and methods employed, yet our value appears in line with these works.

Regardless, this is where the literature ends; with functional connectivity. Compared to the timeseries approaches that perform better, this indicates that there is important temporal dynamics useful for behavior score prediction that is lost. Shifting to model-based timeseries methods, I-ICA improves over the FCM baseline by learning the distinct sources that compose the BOLD data leading a MoCA value of $R = 0.14$. However, since the sources are independent across subjects, this individual approach lacks group level information useful for forming shared sources among individuals. Thus, the G-ICA method with $R = 0.18$, provides an advantage to finding shared sources at the population level. Yet, the ALFF approach ends up being the best *model-based* method with $R = 0.20$.

However, these previous approaches use *model-based* feature extraction that may not be optimally relevant for behavior score prediction. By comparison, the deep learning methods

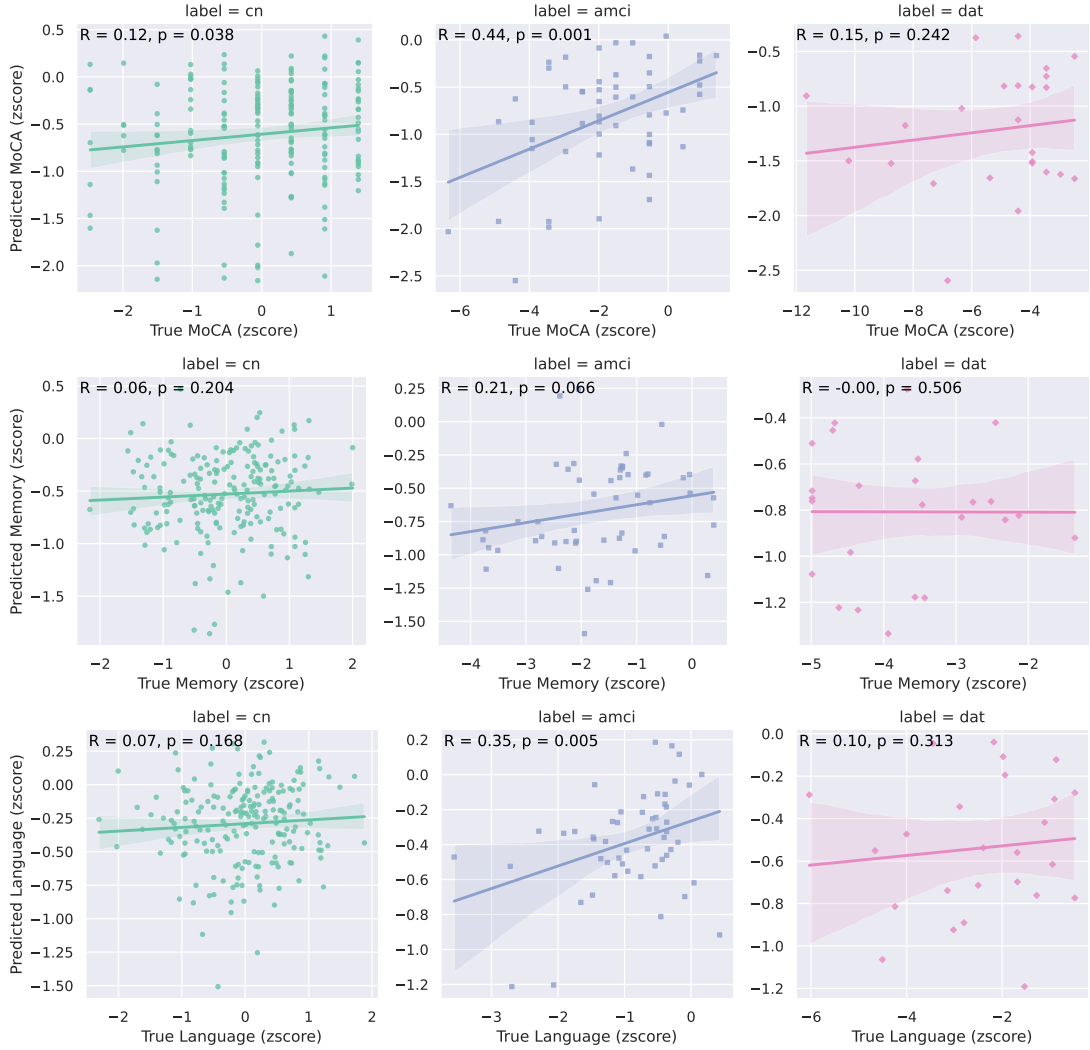


Fig. 3: Correlation scatter plots displaying the relationship between predicted NeuroMamba scores and true behavioral metrics (rows), across the Alzheimer’s disease spectrum (columns), presented in z-score normalized space.

Method	MoCA	Memory	Language
Mamba	0.23***	0.12*	0.19***
+bidirectionality	0.28***	0.18**	0.19***
+differential	0.34***	0.24***	0.22***
+SBR = NeuroMamba	0.36***	0.24***	0.25***

TABLE IV: Comparative ablation analysis illustrating the performance differences between NeuroMamba and the standard Mamba architecture.

performed relatively well with values within $R = 0.19 - 0.28$. Shifting to NeuroMamba, our *data-driven* multivariate timeseries method, it achieved the highest value $R = 0.36$, indicating superior capability in learning temporal dynamics.

2) Ablation Study: The ablation analysis, shown in Table IV, compares NeuroMamba relative to the standard Mamba architecture. These results reveal progressive improvements in predictive accuracy across cognitive categories. The bidirectional component with non-causal design leads to a 22% improvement for MoCA relative to Mamba by better capturing long-range dependencies and patterns in the complex

data. Further, the differential component leads to a 11% improvement relative to the bidirectional Mamba variant by amplifying “attention” to related brain regions relevant for prediction. Finally, using small batch regularization (SBR) as a training technique leads to a 10% improvement relative to the differential variant, showcasing the use of this implicit regularization technique to prevent overfitting by introducing noisy gradient updates for better generalization.

3) Behavior Score Plots: The predicted behavior scores are computed for the entire dataset and plotted against the true behavior scores in Fig. 3 for the NeuroMamba model with reported (R, p) -values for each behavior score and disease categories. Across the behavior scores, the highest correlation values are achieved for the amnestic MCI group, indicating its potential for at-risk populations that may develop into the DAT variety.

4) Impactful Brain Regions: The NeuroMamba backbone $\mathcal{P}(f_\theta(X^i)) = h^i \in \mathbb{R}^B$ extracts B elements, one element for each brain region in the list of Power atlas ROIs. This is fed to an affine layer $g_\theta(h^i) = W_\theta h^i + b_\theta$ to pick out

PFI (RMSE)	Power ROI	MNI (x,y,z)	Nominal System	Lobe/Area	Talairach Daemon Label
MoCA					
1.84	77	(-13, -40, 1)	Default Mode	Limbic Cortex	Parahippocampal Gyrus
0.39	170	(6, -81, 6)	Visual	Occipital Lobe	Cuneus
0.21	177	(-53, -49, 43)	Fronto-parietal Task Control	Parietal Lobe	Inferior Parietal Lobule
0.07	212	(-11, 26, 25)	Salience	Limbic Cortex	Anterior Cingulate
0.05	93	(15, -63, 26)	Default Mode	Occipital Lobe	Precuneus
Memory					
1.62	77	(-13, -40, 1)	Default Mode	Limbic Cortex	Parahippocampal Gyrus
0.27	177	(-53, -49, 43)	Fronto-parietal Task Control	Parietal Lobe	Inferior Parietal Lobule
0.26	111	(-11, 45, 8)	Default Mode	Limbic Cortex	Anterior Cingulate
0.22	170	(6, -81, 6)	Visual	Occipital Lobe	Cuneus
0.15	93	(15, -63, 26)	Default Mode	Occipital Lobe	Precuneus
Language					
0.79	77	(-13, -40, 1)	Default Mode	Limbic Cortex	Parahippocampal Gyrus
0.60	221	(2, -24, 30)	Emotion/Behavior	Limbic Cortex	Cingulate Gyrus
0.30	170	(6, -81, 6)	Visual	Occipital Lobe	Cuneus
0.26	177	(-53, -49, 43)	Fronto-parietal Task Control	Parietal Lobe	Inferior Parietal Lobule
0.26	19	(13, -33, 75)	Sensory/Motor	Frontal Lobe	Precentral Gyrus

TABLE V: Top five brain regions implicated in behavior score prediction, ranked by importance using permutation feature importance (PFI) for each score category. Additional columns provide MNI coordinates, nominal system category, lobe classification, and Talairach Daemon (TD) labels.

some sparse combination of brain regions that are useful for prediction. In a standard linear regression problem, where all of the features are z-score normalized, one can use the learned magnitude weights in W to directly rank which features are most impactful. However, in the deep learning context, this condition is not necessarily met which necessitates more advanced approaches to find the impactful features.

In this work, permutation feature importance (PFI) [56] is used to aid in this problem. PFI is a method used to determine the significance of different features in any black box model by measuring how much the prediction error increases when the values of a single feature are randomly shuffled among samples. If shuffling a feature significantly worsens the accuracy of the model, then that feature is considered important for the prediction task. This is done for each element in $h \in \mathbb{R}^B$ independently over 100 shuffling trials while holding the other features fixed. The PFI method is applied for each behavior score category to identify relevant brain regions. The root mean square error (RMSE) metric is used to measure model performance degradation, and the top 5 brain regions for each behavior score is shown in Table V. Additionally, the Power atlas ROI index, MNI-space coordinates, nominal system, lobe/area, and Talairach Daemon labels [57] are included for each brain region to enhance discussion.

For brevity, only MoCA related brain regions are discussed here. The top 5 brain regions selected are the parahippocampal gyrus, cuneus, inferior parietal lobule, anterior cingulate, and precuneus. The parahippocampal gyrus is important for memory encoding, retrieval, spatial navigation, and contextual processing [58]. For AD subjects, the parahippocampal gyrus shows atrophy with decline in episodic memory [59], reduced

activation during memory tasks in fMRI [60], early deposition of amyloid-beta plaques and tau proteins [61], and is considered a key node in the DMN with disrupted connectivity [62]. Because of this, it is not surprising that this region was extremely impactful. The cuneus, a region on the occipital lobe responsible for higher-order visual processing, has been implicated in cognitive impairment by atrophy and hypometabolism that are associated with deficits in visual processing, spatial navigation, and attentional functions in AD subjects [63]–[65]. The precuneus is a region with many daydreaming-like functions such as mental imagery, episodic memory, self-reflection, and it is an active part of the DMN in rs-fMRI [66]. Similarly, the precuneus shows reduced metabolism and atrophy in AD subjects [67], [68]. The inferior parietal lobule (IPL) is involved in various cognitive processes such as speech, language, spatial reasoning, working memory, and number processing [69]. The IPL undergoes changes in the thickness of its banks during the transition from healthy to mild impairment [70], and abnormal functional connectivity changes occur with respect to other networks such as salience, sensorimotor, and executive [71]. Lastly, the anterior cingulate (ACC) plays a major role in emotion regulation and processing like impulse control, motivation, goal-directed behavior, and emotional pain perception [72]. For AD subjects, the ACC exhibits reduced thickness [73] and decreased functional connectivity [74], which has connections to high agitation, irritability, and anxiety in people with AD [75]. To summarize, our findings of relevant brain regions for behavior score prediction in rs-fMRI closely align with established medical research on impaired regions in AD; which may be useful for intervention strategies such as multi-region HD-tDCS applications.

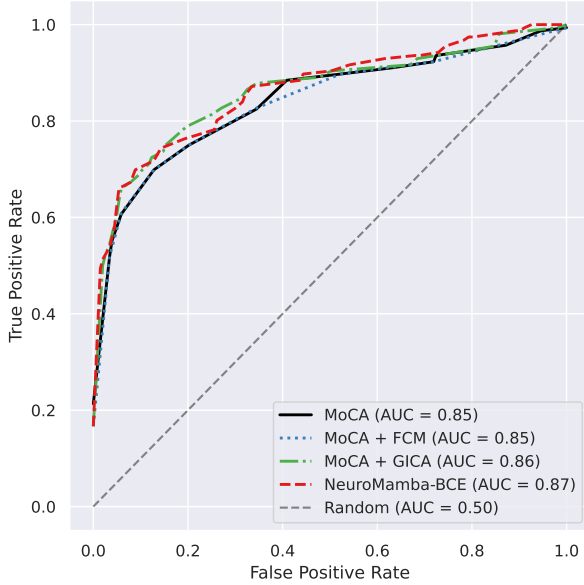


Fig. 4: Receiver operating characteristic (ROC) curve with area under curve (AUC) values for diagnosis between cognitively normal and non-normal subjects.

5) Early Biomarker Feasibility: There have been many works that explore classification/diagnosis of subjects in the AD spectrum using rs-fMRI data [76]–[81]. They all follow the same general formula: 1) introduce the idea that functional changes occur in the brain earlier than structural ones meaning there is promise for early diagnosis, 2) develop some novelty in the methodology, e.g., going from a convolutional to a transformer-based network, that performs relatively better for diagnosis, and 3) reiterate that these results indicate the potential for rs-fMRI data to be used as an early biomarker for diagnosis. However, these works and many others miss the mark. The more interesting question is whether rs-fMRI data adds something useful for diagnosis that does not already exist in easily acquired metrics such as MoCA. In this experiment, we aim to analyze the classification performance of {only using MoCA, MoCA with FCM features, MoCA with G-ICA features, and MoCA with the proposed NeuroMamba model}. For the model-based approaches, logistic regression is used to predict the probability of belonging in the positive class (aMCI and DAT) from the negative class (CN). For NeuroMamba, a variant named NeuroMamba-BCE is created that combines the backbone model f_θ with MoCA values s by

NeuroMamba-BCE

$$f_\theta(\cdot) = \mathcal{P}([\text{Mamba}++_\theta^{(l)}(\cdot) \text{ for } l = 1 \dots L]) \quad (14)$$

$$g_\theta(\cdot, s^i) = W_\theta \text{Concat}[f_\theta(\cdot); \underbrace{s^i}_{\text{rs-fMRI features}}] + b_\theta \quad (15)$$

$$\min_\theta \sum_{i=1}^N \underbrace{\mathcal{L}_{\text{BCE}}(g_\theta(X^i, s^i); c^i)}_{\text{binary cross entropy}} + \lambda \underbrace{\|f_\theta(X^i)\|_1}_{\text{sparsity reg.}} \quad (16)$$

and train the model using the binary cross entropy loss function to learn the mapping between features $\{X^i, s^i\}$ and subject label c^i . Since it directly predicts probabilities, logistic regression is not needed here in this deep approach.

The receiver operating characteristic (ROC) curve is plotted in Fig. 4 for these approaches along with area under curve (AUC) values. From these results, there was no improvement in diagnostic ability across connectivity and timeseries-based methods; including our proposed model. This negative result indicates that *resting-state* fMRI is unlikely to provide additional diagnostic power that is not already existent in MoCA and other readily available metrics. However, it is possible that *task-based* fMRI could provide more complementary information given it is more likely to better “stress” the brain networks. Further research is necessary to conclusively determine whether fMRI as a whole is beneficial for early diagnosis.

6) Out of Distribution (OOD) Generalization: The Alzheimer’s Disease Neuroimaging Initiative (ADNI) [82] group began in 2004 with the main goals being to provide data to researchers and improve doctor diagnosis of subjects with AD. Part of this data collection includes the MoCA exam and 3T rs-fMRI EPI data (Flip Angle=90°, TE=30ms, TR=3.0s, 3.4mm spatial resolution, 192 total time samples) which gives us an opportunity to explore how these methods generalize to a different dataset. The ADNI dataset is prepared following a similar methodology as Sec. II-C with a few key differences. Namely, fieldmap data is inconsistent and missing for some subjects so fieldmap-less susceptibility distortion correction is done instead. Additionally, since the TR is quite high, slice timing correction is needed to ensure that all slices are treated as if they were acquired simultaneously. The MoCA scores are z-score normalized per the MADRC normal population. The ADNI data consists of 471 subjects (324 CN, 110 aMCI, 37 DAT) over 860 sessions (579 CN, 220 aMCI, 61 DAT). Care is taken to ensure no leakage during testing, i.e., a subject’s scans are held out entirely rather than session only.

In this section, we test for two things: zero-shot transfer and all-shot training. Zero-shot means a method is trained on MADRC and tested on ADNI using the same hyperparameters from MADRC. All-shot means trained on ADNI directly using the same hyperparameters from MADRC. The ADNI data contains 192 time samples with a TR = 3.0s whereas MADRC data contains 570 time samples with a TR = 0.8s. Therefore, this section explores the effect of temporal resolution on predictive accuracy of MoCA, and other key differences between the two data distributions. Similar to Sec. V-B.1, Table VI shows MoCA R values for the ADNI data under the zero-shot and all-shot settings.

Functional connectivity appears unaffected in both scenarios, likely due to its independence from temporal dynamics. The model-based timeseries methods did not exhibit strong zero-shot transfer nor all-shot performance, with G-ICA being the one notable exception, indicating the ideal hyperparameters are some function of temporal resolution. Shifting to data-driven timeseries methods, for PatchTST and TCN, these models showed weak zero-shot and all-shot performance likely

Method	Zero-shot	All-shot
FCM + KRR	0.12***	0.12***
I-ICA + KRR	0.04	0.05*
G-ICA + KRR	0.03	0.29***
ALFF + KRR	0.05	0.01*
TCN	0.09**	0.16***
BiLSTM	0.12***	0.29***
PatchTST	0.08**	0.08**
NeuroMamba	0.17***	0.36***

TABLE VI: Out of domain (OOD) generalization on Alzheimer’s Disease Neuroimaging Initiative (ADNI) dataset where values indicate MoCA Pearson correlation. Asterisks denote statistical significance as follows: * = $p < 0.1$, ** = $p < 0.01$, *** = $p < 0.001$.

NeuroMamba	MoCA
Zero-shot	0.17***
Single-shot	0.22***
Three-shot	0.30***
Five-shot	0.35***
All-shot	0.36***

TABLE VII: Domain adaptation on Alzheimer’s Disease Neuroimaging Initiative (ADNI) dataset where values indicate MoCA Pearson correlation. Asterisks denote statistical significance as follows: * = $p < 0.1$, ** = $p < 0.01$, *** = $p < 0.001$.

because the ideal patch size depends on the temporal resolution and kernel sizes. The NeuroMamba model exhibited the strongest zero-shot transfer out of all methods with $R = 0.17$ showing the most robustness to the temporal sampling effects, matching literature observations comparing SSMs to other models [45]. When trained directly on ADNI, NeuroMamba achieved the highest all-shot performance with $R = 0.36$ indicating the model’s strong generalizability to other datasets.

7) Domain Adaptation: For NeuroMamba, per the results in Sec. V-B.6, there is a gap between zero-shot $R = 0.17$ and all-shot $R = 0.36$ values. This provides an opportunity to study whether or not it is possible to close the gap by learning on a tiny subset of ADNI data given the pretrained MADRC model to adjust for any distribution mismatch. In the literature, there are many ways of doing this such as finetuning, freezing the backbone and only updating the last few layers, or by deep learning approaches such as correlation alignment (CORAL) [83] designed to minimize covariance differences between domains. In this setting, we found great success in simply finetuning the pretrained model. As observed in Table VII, with only 5 subjects per class for training data, NeuroMamba achieves a $R = 0.35$ value, nearly matching all-shot performance. This finding shows the model’s ability to correctly adapt to a different domain given very limited training data which is highly practical for many fMRI-related applications.

VI. CONCLUSION

In this work, we sought to advance the understanding and prediction of cognitive performance in AD by leveraging rs-fMRI data with behavioral scores such as MoCA, average memory, and average language metrics. By systematically evaluating the predictive power of both functional connectivity and multivariate timeseries data, we addressed limitations in prior studies which focused exclusively on functional connectivity. Our deep learning approach, based on state space modeling, demonstrated superior performance in predicting behavioral metrics, underscoring the value of temporal dynamics present in rs-fMRI data. Furthermore, NeuroMamba achieved remarkable few-shot transfer performance on ADNI data indicating that only a few subjects are needed when finetuning the MADRC pretrained model to out of domain datasets such as ADNI which is important for real-world usability. These results highlight the potential for integrating machine learning with neuroimaging for early intervention of cognitive decline by techniques such as HD-tDCS while simultaneously offering deeper biological insights into AD progression.

However, there are limitations with this proposed approach. The R values across the behavior scores are modest, indicating possible limitations with using *resting-state* fMRI to analyze cognition scores. It is likely that *task-based* fMRI, where a patient performs some task under the scanner, could better “stress” the networks in the brain revealing a more significant relationship between key regions and behavior metrics. For future work, one can explore face name association [84] and object location association [85] tasks within a *task-based* functional MRI framework to compare against the findings in this work and gain more insights by systematically contrasting resting-state and task-based functional activity.

REFERENCES

- [1] D. A. Orringer, D. R. Vago, and A. J. Golby, “Clinical applications and future directions of functional mri,” in *Seminars in neurology*, vol. 32, no. 04. Thieme Medical Publishers, 2012, pp. 466–475.
- [2] R. L. Buckner, F. M. Krienen, and B. T. Yeo, “Opportunities and limitations of intrinsic functional connectivity mri,” *Nature neuroscience*, vol. 16, no. 7, pp. 832–837, 2013.
- [3] B. Biswal, F. Zerrin Yetkin, V. M. Haughton, and J. S. Hyde, “Functional connectivity in the motor cortex of resting human brain using echo-planar mri,” *Magnetic resonance in medicine*, vol. 34, no. 4, pp. 537–541, 1995.
- [4] S. J. Peltier and Y. Shah, “Biophysical modulations of functional connectivity,” *Brain connectivity*, vol. 1, no. 4, pp. 267–277, 2011.
- [5] E. M. Lake, E. S. Finn, S. M. Noble, T. Vanderwal, X. Shen, M. D. Rosenberg, M. N. Spann, M. M. Chun, D. Scheinost, and R. T. Constable, “The functional brain organization of an individual allows prediction of measures of social abilities transdiagnostically in autism and attention-deficit/hyperactivity disorder,” *Biological psychiatry*, vol. 86, no. 4, pp. 315–326, 2019.
- [6] M. D. Rosenberg, E. S. Finn, D. Scheinost, X. Papademetris, X. Shen, R. T. Constable, and M. M. Chun, “A neuromarker of sustained attention from whole-brain functional connectivity,” *Nature neuroscience*, vol. 19, no. 1, pp. 165–171, 2016.
- [7] M. D. Greicius, B. Krasnow, A. L. Reiss, and V. Menon, “Functional connectivity in the resting brain: a network analysis of the default mode hypothesis,” *Proceedings of the national academy of sciences*, vol. 100, no. 1, pp. 253–258, 2003.
- [8] M. E. Raichle, A. M. MacLeod, A. Z. Snyder, W. J. Powers, D. A. Gusnard, and G. L. Shulman, “A default mode of brain function,” *Proceedings of the national academy of sciences*, vol. 98, no. 2, pp. 676–682, 2001.

- [9] C. R. Jack Jr, D. A. Bennett, K. Blennow, M. C. Carrillo, B. Dunn, S. B. Haeberlein, D. M. Holtzman, W. Jagust, F. Jessen, J. Karlawish *et al.*, “Nia-aa research framework: toward a biological definition of alzheimer’s disease,” *Alzheimer’s & dementia*, vol. 14, no. 4, pp. 535–562, 2018.
- [10] M. C. Kroes, M. D. Rugg, M. G. Whalley, and C. R. Brewin, “Structural brain abnormalities common to posttraumatic stress disorder and depression,” *Journal of Psychiatry and Neuroscience*, vol. 36, no. 4, pp. 256–265, 2011.
- [11] Z. S. Nasreddine, N. A. Phillips, V. Bédirian, S. Charbonneau, V. Whitehead, I. Collin, J. L. Cummings, and H. Chertkow, “The montreal cognitive assessment, moca: a brief screening tool for mild cognitive impairment,” *Journal of the American Geriatrics Society*, vol. 53, no. 4, pp. 695–699, 2005.
- [12] K. Zukotynski, V. Gaudet, P. H. Kuo, S. Adamo, M. Goubran, C. J. Scott, C. Bocti, M. Borrie, H. Chertkow, R. Frayne *et al.*, “The use of random forests to identify brain regions on amyloid and fdg pet associated with moca score,” *Clinical nuclear medicine*, vol. 45, no. 6, pp. 427–433, 2020.
- [13] C. Liu, L. Li, D. Zhu, S. Lin, L. Ren, W. Zhen, W. Tan, L. Wang, L. Tian, Q. Wang *et al.*, “Individualized prediction of cognitive test scores from functional brain connectome in patients with first-episode late-life depression,” *Journal of Affective Disorders*, vol. 352, pp. 32–42, 2024.
- [14] X. Shen, E. S. Finn, D. Scheinost, M. D. Rosenberg, M. M. Chun, X. Papademetris, and R. T. Constable, “Using connectome-based predictive modeling to predict individual behavior from brain connectivity,” *nature protocols*, vol. 12, no. 3, pp. 506–518, 2017.
- [15] Q. Lin, M. D. Rosenberg, K. Yoo, T. W. Hsu, T. P. O’Connell, and M. M. Chun, “Resting-state functional connectivity predicts cognitive impairment related to alzheimer’s disease,” *Frontiers in aging neuroscience*, vol. 10, p. 94, 2018.
- [16] W. G. Rosen, R. C. Mohs, and K. L. Davis, “A new rating scale for alzheimer’s disease,” *The American journal of psychiatry*, vol. 141, no. 11, pp. 1356–1364, 1984.
- [17] M. Karker, “Predictive analysis and deep learning of functional mri in alzheimer’s disease,” Ph.D. dissertation, University of Michigan, 2022.
- [18] B. M. Hampstead, A. Iordan, A. Rahman-Filiapiak, R. Ploutz-Snyder, and P. Pruitt, “Synergistic effects of cognitive training and high-definition transcranial direct current stimulation across the dementia spectrum,” *Brain Stimulation: Basic, Translational, and Clinical Research in Neuromodulation*, vol. 18, no. 1, p. 350, 2025.
- [19] S. Weintraub, D. Salmon, N. Mercaldo, S. Ferris, N. R. Graff-Radford, H. Chui, J. Cummings, C. DeCarli, N. L. Foster, D. Galasko *et al.*, “The alzheimer’s disease centers’ uniform data set (uds): the neuropsychologic test battery,” *Alzheimer Disease & Associated Disorders*, vol. 23, no. 2, pp. 91–101, 2009.
- [20] C. O. Nester, J. Qin, C. Wang, M. J. Katz, R. B. Lipton, and L. A. Rabin, “Concordance between logical memory and craft story 21 in community-dwelling older adults: the role of demographic factors and cognitive status,” *Archives of Clinical Neuropsychology*, vol. 38, no. 7, pp. 1091–1105, 2023.
- [21] A. Stasenko, D. M. Jacobs, D. P. Salmon, and T. H. Gollan, “The multilingual naming test (mint) as a measure of picture naming ability in alzheimer’s disease,” *Journal of the International Neuropsychological Society*, vol. 25, no. 8, pp. 821–833, 2019.
- [22] K. J. Gorgolewski, T. Auer, V. D. Calhoun, R. C. Craddock, S. Das, E. P. Duff, G. Flandin, S. S. Ghosh, T. Glatard, Y. O. Halchenko *et al.*, “The brain imaging data structure, a format for organizing and describing outputs of neuroimaging experiments,” *Scientific data*, vol. 3, no. 1, pp. 1–9, 2016.
- [23] O. Esteban, C. J. Markiewicz, R. W. Blair, C. A. Moodie, A. I. Isik, A. Erramuzpe, J. D. Kent, M. Goncalves, E. DuPre, M. Snyder *et al.*, “fmriprep: a robust preprocessing pipeline for functional mri,” *Nature methods*, vol. 16, no. 1, pp. 111–116, 2019.
- [24] R. Ciric, R. Lorenz, W. Thompson, M. Goncalves, E. MacNicol, C. J. Markiewicz, Y. O. Halchenko, S. S. Ghosh, K. J. Gorgolewski, R. A. Poldrack *et al.*, “Templateflow: a community archive of imaging templates and atlases for improved consistency in neuroimaging,” *bioRxiv*, pp. 2021–02, 2021.
- [25] S. Whitfield-Gabrieli and A. Nieto-Castanon, “Conn: a functional connectivity toolbox for correlated and anticorrelated brain networks,” *Brain connectivity*, vol. 2, no. 3, pp. 125–141, 2012.
- [26] J. D. Power, A. L. Cohen, S. M. Nelson, G. S. Wig, K. A. Barnes, J. A. Church, A. C. Vogel, T. O. Laumann, F. M. Miezin, B. L. Schlaggar *et al.*, “Functional network organization of the human brain,” *Neuron*, vol. 72, no. 4, pp. 665–678, 2011.
- [27] G. C. McDonald, “Ridge regression,” *Wiley Interdisciplinary Reviews: Computational Statistics*, vol. 1, no. 1, pp. 93–100, 2009.
- [28] V. Vovk, “Kernel ridge regression,” in *Empirical inference: Festschrift in honor of vladimir n. vapnik*. Springer, 2013, pp. 105–116.
- [29] B. Schölkopf and A. J. Smola, *Learning with kernels: support vector machines, regularization, optimization, and beyond*. MIT press, 2002.
- [30] A. Hyvärinen and E. Oja, “Independent component analysis: algorithms and applications,” *Neural networks*, vol. 13, no. 4-5, pp. 411–430, 2000.
- [31] V. D. Calhoun, T. Adali, G. D. Pearson, and J. J. Pekar, “A method for making group inferences from functional mri data using independent component analysis,” *Human brain mapping*, vol. 14, no. 3, pp. 140–151, 2001.
- [32] C. F. Beckmann, M. DeLuca, J. T. Devlin, and S. M. Smith, “Investigations into resting-state connectivity using independent component analysis,” *Philosophical Transactions of the Royal Society B: Biological Sciences*, vol. 360, no. 1457, pp. 1001–1013, 2005.
- [33] L. Griffanti, G. Douaud, J. Bijsterbosch, S. Evangelisti, F. Alfaro-Almagro, M. F. Glasser, E. P. Duff, S. Fitzgibbon, R. Westphal, D. Carone *et al.*, “Hand classification of fmri ica noise components,” *Neuroimage*, vol. 154, pp. 188–205, 2017.
- [34] V. D. Calhoun, J. Liu, and T. Adali, “A review of group ica for fmri data and ica for joint inference of imaging, genetic, and erp data,” *Neuroimage*, vol. 45, no. 1, pp. S163–S172, 2009.
- [35] V. J. Schmithorst and S. K. Holland, “Comparison of three methods for generating group statistical inferences from independent component analysis of functional magnetic resonance imaging data,” *Journal of Magnetic Resonance Imaging: An Official Journal of the International Society for Magnetic Resonance in Medicine*, vol. 19, no. 3, pp. 365–368, 2004.
- [36] L. Yang, Y. Yan, Y. Wang, X. Hu, J. Lu, P. Chan, T. Yan, and Y. Han, “Gradual disturbances of the amplitude of low-frequency fluctuations (alff) and fractional alff in alzheimer spectrum,” *Frontiers in neuroscience*, vol. 12, p. 975, 2018.
- [37] J.-J. Wang, X. Chen, S. Sah, C. Zeng, Y.-M. Li, N. Li, M.-Q. Liu, and S.-L. Du, “Amplitude of low-frequency fluctuation (alff) and fractional alff in migraine patients: a resting-state functional mri study,” *Clinical radiology*, vol. 71, no. 6, pp. 558–564, 2016.
- [38] R. Yu, Y.-L. Chien, H.-L. S. Wang, C.-M. Liu, C.-C. Liu, T.-J. Hwang, M. H. Hsieh, H.-G. Hwu, and W.-Y. I. Tseng, “Frequency-specific alternations in the amplitude of low-frequency fluctuations in schizophrenia,” *Human brain mapping*, vol. 35, no. 2, pp. 627–637, 2014.
- [39] S. Bai, J. Z. Kolter, and V. Koltun, “An empirical evaluation of generic convolutional and recurrent networks for sequence modeling,” in *The Sixth International Conference on Learning Representations (ICLR)*, 2018.
- [40] A. Sherstinsky, “Fundamentals of recurrent neural network (rnn) and long short-term memory (lstm) network,” *Physica D: Nonlinear Phenomena*, vol. 404, p. 132306, 2020.
- [41] A. Graves, S. Fernández, and J. Schmidhuber, “Bidirectional lstm networks for improved phoneme classification and recognition,” in *International conference on artificial neural networks*. Springer, 2005, pp. 799–804.
- [42] Y. Nie, N. H. Nguyen, P. Sinthong, and J. Kalagnanam, “A time series is worth 64 words: Long-term forecasting with transformers,” in *The Eleventh International Conference on Learning Representations (ICLR)*, 2023.
- [43] A. Vaswani, N. Shazeer, N. Parmar, J. Uszkoreit, L. Jones, A. N. Gomez, L. Kaiser, and I. Polosukhin, “Attention is all you need,” *Advances in neural information processing systems*, vol. 30, 2017.
- [44] M. Aoki, *State space modeling of time series*. Springer Science & Business Media, 2013.
- [45] A. Gu, K. Goel, and C. Re, “Efficiently modeling long sequences with structured state spaces,” in *International Conference on Learning Representations*, 2022.
- [46] A. Gu and T. Dao, “Mamba: Linear-time sequence modeling with selective state spaces,” in *International Conference on Learning Representations*, 2024.
- [47] T. Dao and A. Gu, “Transformers are ssms: Generalized models and efficient algorithms through structured state space duality,” in *International Conference on Machine Learning*. PMLR, 2024, pp. 10041–10071.
- [48] G. E. Blelloch, “Prefix sums and their applications,” *Carnegie Mellon University Pittsburgh, PA, USA*, 1990.
- [49] A. Gu, T. Dao, S. Ermon, A. Rudra, and C. Ré, “Hippo: Recurrent memory with optimal polynomial projections,” *Advances in neural information processing systems*, vol. 33, pp. 1474–1487, 2020.

- [50] T. Ye, L. Dong, Y. Xia, Y. Sun, Y. Zhu, G. Huang, and F. Wei, “Differential transformer,” in *The Thirteenth International Conference on Learning Representations*, 2025.
- [51] N. Schneider, I. Zimerman, and E. Nachmani, “Differential mamba,” in *Association for Computational Linguistics (ACL)*, 2025.
- [52] D. Lei, Z. Sun, Y. Xiao, and W. Y. Wang, “Implicit regularization of stochastic gradient descent in natural language processing: Observations and implications,” *arXiv preprint arXiv:1811.00659*, 2018.
- [53] D. Masters and C. Luschi, “Revisiting small batch training for deep neural networks,” *arXiv preprint arXiv:1804.07612*, 2018.
- [54] A. Sekhari, K. Sridharan, and S. Kale, “Sgd: The role of implicit regularization, batch-size and multiple-epochs,” *Advances In Neural Information Processing Systems*, vol. 34, pp. 27422–27433, 2021.
- [55] B. Zhang and R. Sennrich, “Root mean square layer normalization,” *Advances in neural information processing systems*, vol. 32, 2019.
- [56] A. Altmann, L. Tolosi, O. Sander, and T. Lengauer, “Permutation importance: a corrected feature importance measure,” *Bioinformatics*, vol. 26, no. 10, pp. 1340–1347, 2010.
- [57] J. L. Lancaster, M. G. Woldorff, L. M. Parsons, M. Liotti, C. S. Freitas, L. Rainey, P. V. Kochunov, D. Nickerson, S. A. Mikiten, and P. T. Fox, “Automated talairach atlas labels for functional brain mapping,” *Human brain mapping*, vol. 10, no. 3, pp. 120–131, 2000.
- [58] A. M. Ward, A. P. Schultz, W. Huijbers, K. R. Van Dijk, T. Hedden, and R. A. Sperling, “The parahippocampal gyrus links the default-mode cortical network with the medial temporal lobe memory system,” *Human brain mapping*, vol. 35, no. 3, pp. 1061–1073, 2014.
- [59] A. Du, N. Schuff, D. Amend, M. Laakso, Y. Hsu, W. Jagust, K. Yaffe, J. Kramer, B. Reed, D. Norman *et al.*, “Magnetic resonance imaging of the entorhinal cortex and hippocampus in mild cognitive impairment and alzheimer’s disease,” *Journal of Neurology, Neurosurgery & Psychiatry*, vol. 71, no. 4, pp. 441–447, 2001.
- [60] K. A. Celone, V. D. Calhoun, B. C. Dickerson, A. Atri, E. F. Chua, S. L. Miller, K. DePeau, D. M. Rentz, D. J. Selkoe, D. Blacker *et al.*, “Alterations in memory networks in mild cognitive impairment and alzheimer’s disease: an independent component analysis,” *Journal of Neuroscience*, vol. 26, no. 40, pp. 10222–10231, 2006.
- [61] H. Braak and E. Braak, “Neuropathological staging of alzheimer-related changes,” *Acta neuropathologica*, vol. 82, no. 4, pp. 239–259, 1991.
- [62] M. D. Greicius, G. Srivastava, A. L. Reiss, and V. Menon, “Default-mode network activity distinguishes alzheimer’s disease from healthy aging: evidence from functional mri,” *Proceedings of the National Academy of Sciences*, vol. 101, no. 13, pp. 4637–4642, 2004.
- [63] M. A. Binnewijzend, M. M. Schoonheim, E. Sanz-Arigita, A. M. Wink, W. M. van der Flier, N. Tolboom, S. M. Adriance, J. S. Damoiseaux, P. Scheltens, B. N. van Berckel *et al.*, “Resting-state fmri changes in alzheimer’s disease and mild cognitive impairment,” *Neurobiology of aging*, vol. 33, no. 9, pp. 2018–2028, 2012.
- [64] H. Yang, H. Xu, Q. Li, Y. Jin, W. Jiang, J. Wang, Y. Wu, W. Li, C. Yang, X. Li *et al.*, “Study of brain morphology change in alzheimer’s disease and amnesia mild cognitive impairment compared with normal controls,” *General psychiatry*, vol. 32, no. 2, p. e100005, 2019.
- [65] M. De Marco, D. Duzzi, F. Meneghelli, and A. Venneri, “Cognitive efficiency in alzheimer’s disease is associated with increased occipital connectivity,” *Journal of Alzheimer’s Disease*, vol. 57, no. 2, pp. 541–556, 2017.
- [66] A. E. Cavanna and M. R. Trimble, “The precuneus: a review of its functional anatomy and behavioural correlates,” *Brain*, vol. 129, no. 3, pp. 564–583, 2006.
- [67] M. Baily, C. Destrieux, C. Hommet, K. Mondon, J.-P. Cottier, E. Beaufilis, E. Vierron, J. Vercouillie, M. Ibazizene, T. Voisin *et al.*, “Precuneus and cingulate cortex atrophy and hypometabolism in patients with alzheimer’s disease and mild cognitive impairment: Mri and 18f-fdg pet quantitative analysis using freesurfer,” *BioMed research international*, vol. 2015, no. 1, p. 583931, 2015.
- [68] G. Karas, P. Scheltens, S. Rombouts, R. Van Schijndel, M. Klein, B. Jones, W. Van Der Flier, H. Vrenken, and F. Barkhof, “Precuneus atrophy in early-onset alzheimer’s disease: a morphometric structural mri study,” *Neuroradiology*, vol. 49, no. 12, pp. 967–976, 2007.
- [69] F. C. Binkofski, J. Klann, and S. Caspers, “On the neuroanatomy and functional role of the inferior parietal lobule and intraparietal sulcus,” in *Neurobiology of language*. Elsevier, 2016, pp. 35–47.
- [70] S. J. Greene, R. J. Killiany, A. D. N. Initiative *et al.*, “Subregions of the inferior parietal lobule are affected in the progression to alzheimer’s disease,” *Neurobiology of aging*, vol. 31, no. 8, pp. 1304–1311, 2010.
- [71] Z. Wang, M. Xia, Z. Dai, X. Liang, H. Song, Y. He, and K. Li, “Differentially disrupted functional connectivity of the subregions of the inferior parietal lobule in alzheimer’s disease,” *Brain Structure and Function*, vol. 220, no. 2, pp. 745–762, 2015.
- [72] F. L. Stevens, R. A. Hurley, and K. H. Taber, “Anterior cingulate cortex: unique role in cognition and emotion,” *The Journal of neuropsychiatry and clinical neurosciences*, vol. 23, no. 2, pp. 121–125, 2011.
- [73] H.-J. Jeong, Y.-M. Lee, J.-M. Park, B.-D. Lee, E. Moon, H. Suh, H.-J. Kim, K. Pak, K.-U. Choi, and Y.-I. Chung, “Reduced thickness of the anterior cingulate cortex as a predictor of amnestic-mild cognitive impairment conversion to alzheimer’s disease with psychosis,” *Journal of Alzheimer’s Disease*, vol. 84, no. 4, pp. 1709–1717, 2021.
- [74] X. Liu, W. Chen, H. Hou, X. Chen, J. Zhang, J. Liu, Z. Guo, and G. Bai, “Decreased functional connectivity between the dorsal anterior cingulate cortex and lingual gyrus in alzheimer’s disease patients with depression,” *Behavioural brain research*, vol. 326, pp. 132–138, 2017.
- [75] S. Tekin, M. S. Mega, D. M. Masterman, T. Chow, J. Garakian, H. V. Vinters, and J. L. Cummings, “Orbitofrontal and anterior cingulate cortex neurofibrillary tangle burden is associated with agitation in alzheimer disease,” *Annals of neurology*, vol. 49, no. 3, pp. 355–361, 2001.
- [76] J. Salazar Cavazos and S. Peltier, “Alzheimers disease classification in functional mri with 4d joint temporal-spatial kernels in novel 4d cnn model,” *arXiv preprint arXiv:2506.02060*, 2025.
- [77] F. de Vos, M. Koini, T. M. Schouten, S. Seiler, J. van der Grond, A. Lechner, R. Schmidt, M. de Rooij, and S. A. Rombouts, “A comprehensive analysis of resting state fmri measures to classify individual patients with alzheimer’s disease,” *Neuroimage*, vol. 167, pp. 62–72, 2018.
- [78] A. Alorf and M. U. G. Khan, “Multi-label classification of alzheimer’s disease stages from resting-state fmri-based correlation connectivity data and deep learning,” *Computers in Biology and Medicine*, vol. 151, p. 106240, 2022.
- [79] F. Ramzan, M. U. G. Khan, A. Rehmat, S. Iqbal, T. Saba, A. Rehman, and Z. Mehmood, “A deep learning approach for automated diagnosis and multi-class classification of alzheimer’s disease stages using resting-state fmri and residual neural networks,” *Journal of medical systems*, vol. 44, no. 2, p. 37, 2020.
- [80] U. Khatri and G.-R. Kwon, “Alzheimer’s disease diagnosis and biomarker analysis using resting-state functional mri functional brain network with multi-measures features and hippocampal subfield and amygdala volume of structural mri,” *Frontiers in aging neuroscience*, vol. 14, p. 818871, 2022.
- [81] J.-H. Noh, J.-H. Kim, and H.-D. Yang, “Classification of alzheimer’s progression using fmri data,” *Sensors*, vol. 23, no. 14, p. 6330, 2023.
- [82] ADNI. (2026) Alzheimer’s disease neuroimaging initiative. [Online]. Available: <https://adni.loni.usc.edu/>
- [83] B. Sun, J. Feng, and K. Saenko, “Correlation alignment for unsupervised domain adaptation,” in *Domain adaptation in computer vision applications*. Springer, 2017, pp. 153–171.
- [84] D. M. Rentz, R. E. Amariglio, J. A. Becker, M. Frey, L. E. Olson, K. Frishe, J. Carmasin, J. E. Maye, K. A. Johnson, and R. A. Sperling, “Face-name associative memory performance is related to amyloid burden in normal elderly,” *Neuropsychologia*, vol. 49, no. 9, pp. 2776–2783, 2011.
- [85] B. M. Hampstead, A. Y. Stringer, R. F. Still, A. Amaraneni, and K. Sathian, “Where did i put that? patients with amnestic mild cognitive impairment demonstrate widespread reductions in activity during the encoding of ecologically relevant object-location associations,” *Neuropsychologia*, vol. 49, no. 9, pp. 2349–2361, 2011.